ADVANCED ENERGY MATERIALS
www.advenergymat.de

Supercapacitor Electrodes Obtained by Directly Bonding 2D MoS_2 on Reduced Graphene Oxide

*Edney Geraldo da Silveira Firmiano, Adriano C. Rabelo, Cleocir J. Dalmaschio, Antonio N. Pinheiro, Ernesto C. Pereira, Wido H. Schreiner, and Edson Robeto Leite**

Layered molybdenum disulfide (MoS_2) is deposited by microwave heating on a reduced graphene oxide (RGO). Three concentrations of MoS_2 are loaded on RGO, and the structure and morphology are characterized. The first layers of MoS_2 are detected as being directly bonded with the oxygen of the RGO by covalent chemical bonds (Mo-O-C). Electrochemical characterizations indicate that this electroactive material can be cycled reversibly between 0.25 and 0.8 V in 1 M $HClO_4$ solution for hybrids with low concentrations of MoS_2 layers ($LCMoS_2$/RGO) and between 0.25 and 0.65 V for medium ($MCMoS_2$/RGO) and high concentrations ($HCMoS_2$/RGO) of MoS_2 layers on graphene. The specific capacitance measured values at 10 mV s^{-1} are 128, 265, and 148 Fg^{-1} for the MoS_2/RGO with low, medium, and high concentrations of MoS_2, respectively, and the calculated energy density is 63 W h kg^{-1} for the $LCMoS_2$/RGO hybrid. This supercapacitor electrode also exhibits superior cyclic stability with 92% of the specific capacitance retained after 1000 cycles.

1. Introduction

Molybdenum disulfide (MoS_2) has been extensively studied for different applications such as catalysts, lubricants, and electrocatalysts for hydrogen evolution reactions, transistors, and cathode materials for lithium batteries.[1–7] Being a typical layered transition metal sulfide, it is composed of three atomic layers (S-Mo-S) stacked together and bonded through van der Waals interactions.[8] This versatility is attributed to its 2D structure, which is analogous to graphene.[9] Much research has been devoted to synthesizing MoS_2 thin layers, including mechanical exfoliation,[10] chemical exfoliation,[9–11] physical vapor deposition,[12] thermal evaporation-exfoliation,[13] hydrothermal synthesis, and solution synthesis.[14–16] However, this material tends to form fullerene-like nanoparticles or nanotube structures during processing.[11] An efficient way to overcome this tendency and synthesize MoS_2 layers is to use the graphene as a substrate.[17–19] The graphene inhibits 3D growth of the MoS_2 crystal during the synthesis process, which results in the formation of layers of MoS_2 over graphene.[17–19] Recently, different research groups demonstrated the possibility of growing MoS_2 layers on graphene by a chemical solution approach.[16–19] Dai et al.[19] developed a solvothermal synthesis of MoS_2 layers on reduced graphene oxide (RGO) sheets using a single compound as the source for Mo and S ($(NH_4)_2MoS_4$) in *N*,*N*-dimethylformamide (DMF). Chen and Chang described another route to process MoS_2/graphene nanosheets using $Na_2MoO_4.2H_2O$ and NH_2CSNH_2 as the Mo and S sources, respectively, in water.[16] In both reports, the chemical bond between the MoS_2 and the graphene sheets was not elucidated.

In addition to the fundamental assistance of the graphene during the synthesis of the composite, the chemical and electronic coupling effect between the MoS_2 and graphene can generate hybrid materials with novel properties. This coupling effect is controlled by the nature of the chemical bond between these compounds.[20] Thus, the identification of this bond is a step toward understanding the electronic and chemical behavior of this hybrid material.

MoS_2 can potentially store charge by intersheet and intrasheet double-layers over individual atomic MoS_2 layers and faradaic charge transfer processes on the Mo center because this atom exhibits several oxidation states, similar to ruthenium.[21] Recently, Ajayan and co-workers have demonstrated a simple and scalable approach to fabricate film-based micro-supercapacitors via spray painting of MoS_2 nanosheets and subsequent laser patterning.[22] These authors showed that the optimum MoS_2-based micro-supercapacitor exhibits excellent electrochemical performance for energy storage with aqueous electrolytes, with a high area capacitance of 8 mF cm^{-2} (volumetric capacitance of 178 F cm^{-3}) and excellent cyclic performance. Soon et al.[21] proposed that MoS_2 sheet-like morphology provides a large surface area for double-layer charge storage; however, a low specific capacitance was observed that is probably related to the low conductivity of the MoS_2 molybdenite phase.[23] Lang et al. have shown that it is possible to overcome this problem in the MnO_2 system using a nanoporous gold template to deposit crystalline MnO_2, which possesses a specific capacitance almost four times higher than those values obtained using pure MnO_2 (1145 F g^{-1} compared to 345 F g^{-1}, respectively).[24] Following a similar strategy, it is

E. G. S. Firmiano, A. C. Rabelo, C. J. Dalmaschio, A. N. Pinheiro, Prof. E. C. Pereira, Prof. E. R. Leite
Chemistry Department
Federal University of São Carlos
São Carlos, SP, Brazil
E-mail: edson.leite@pq.cnpq.br
Prof. W. H. Schreiner
Physics Department
Federal University of Paraná
Curitiba, PR, Brazil

DOI: 10.1002/aenm.201301380

possible to use graphene as a template to grow MoS_2 layers. Graphene is a 2D material and exhibits very high electrical conductivity with a theoretical specific surface area of 2630 m^2 g^{-1} and a high chemical stability.[25] Thus, it could be an interesting substrate to improve the MoS_2 charge-storage capacity. Using graphene as a substrate for MoS_2 layers can facilitate electron transport through MoS_2 nanostructures, which provides an easier and faster ion diffusion between MoS_2 layers/electrolytes and produces high specific capacitance values. The combination of both materials can create an innovative material that can be applied as a promising electrochemical supercapacitor.

In previous research, our group reported a versatile chemical route to deposit layers of MoS_2 on graphene by merging the microwave synthesis approach with an extension of the non-hydrolytic sol-gel method.[1] Here, we explore two main issues related to the MoS_2/graphene hybrid material synthesized by this route. First, we elucidate the type of chemical bond between the MoS_2 layers and RGO. Moreover, we demonstrate that MoS_2 layers grown on RGO exhibit high-performance charge storage properties with high specific capacitance and high energy density. The impressive capacitive behavior reported for the MoS_2/graphene hybrid material probably arises from the combination of faradic and non-faradic processes of the active MoS_2 layers coupled with highly conductive graphene sheets.

2. Results and Discussion

2.1. Growth of MoS_2 Layers on Reduced Graphene Oxide

The MoS_2/graphene hybrid material studied in this research was synthesized by a novel route that allows for selective growth of MoS_2 layers on the graphene surface. Basically, the key point of this route is to use graphene oxide (GO) as hot spot substrates in a microwave irradiation process. At the end of the procedure, MoS_2 layers are deposited over a conductive RGO (MoS_2/RGO) without the need for any further treatment because it is well established that microwave irradiation promotes the partial reduction of GO.[1,26,27]

As described previously,[1] during the MoS_2/RGO hybrid material synthesis, the reaction between butyl mercaptan and $MoCl_5$ under microwave irradiation occurs over the GO surface to form MoS_2 via alkyl halide and/or thioether elimination. We also demonstrated that it is possible to control the [MoS_2]/[RGO] ratio and the degree of the covering of RGO layers by controlling the [Mo and S precursor]/[GO] ratio during the synthesis. Here, we synthesized the MoS_2/RGO hybrid with three different [MoS_2]/[RGO] ratios. The concentration of MoS_2 was measured by thermogravimetric analyses. The material with the lowest [MoS_2]/[RGO] ratio showed a concentration of 5.6 wt% of MoS_2 (labeled LCMoS_2/RGO). The hybrid material with an intermediary [MoS_2]/[RGO] ratio showed a concentration of 17.6 wt% of MoS_2 (labeled MCMoS_2/RGO) and the material with the highest [MoS_2]/[RGO] ratio has a concentration of 44.5 wt% of MoS_2 (labeled HCMoS_2/RGO).

To obtain a detailed phase, morphological, and chemical characterization of the hybrid MoS_2/RGO materials with different MoS_2 concentrations, we performed X-ray diffraction (XRD), transmission electron microscopy (TEM), high-resolution TEM (HRTEM), and X-ray photoelectron spectroscopy (XPS) analyses. XRD analysis showed that the growth of 3D MoS_2 crystals was not visible, even for the HCMoS_2/RGO sample, which indicates that the materials formed over the RGO sheets were layers of MoS_2 (see Figure S1 in the Supporting Information). The selected area electron diffraction (SAED) analysis showed patterns typical of polycrystalline materials (indicated by rings) that were indexed as the hexagonal 2H-MoS_2 phase, which confirms the formation of this sulfide over RGO sheets (see Figure S2 in the Supporting Information). The SAED analysis also indicated the growth of MoS_2 layers textured along the [001] direction over RGO sheets, which resulted in a 2D material. A more detailed analysis of the SAED patterns shows different features for the hybrid materials with different [MoS_2]/[RGO] ratios (see Figure S2 in the Supporting Information). For instance, the SAED pattern of the LCMoS_2/RGO material (see Figure S2c, Supporting Information) showed a broad and discontinuous ring relative to the (100) and (110) planes, which indicates the formation of an oriented MoS_2 island along the [001] direction and a low degree of orientation in relation to the [hk0] direction. On the other hand, the SAED pattern of the HCMoS_2/RGO hybrid material (see Figure S2a, Supporting Information) showed (103) and (105) diffraction planes, which indicates a stacking of several MoS_2 layers. MCMoS_2/RGO materials revealed a SAED pattern (see Figure S2b, Supporting Information) formed by well-defined rings of the (100) and (110) planes, which indicates the formation of layers of MoS_2 over RGO without any preferential orientation in relation to the [hk0] direction.

HRTEM analysis elucidated the morphology of the MoS_2/RGO hybrid materials with different [MoS_2]/[RGO] ratios. As illustrated in the HRTEM images shown in **Figure 1**a–c,

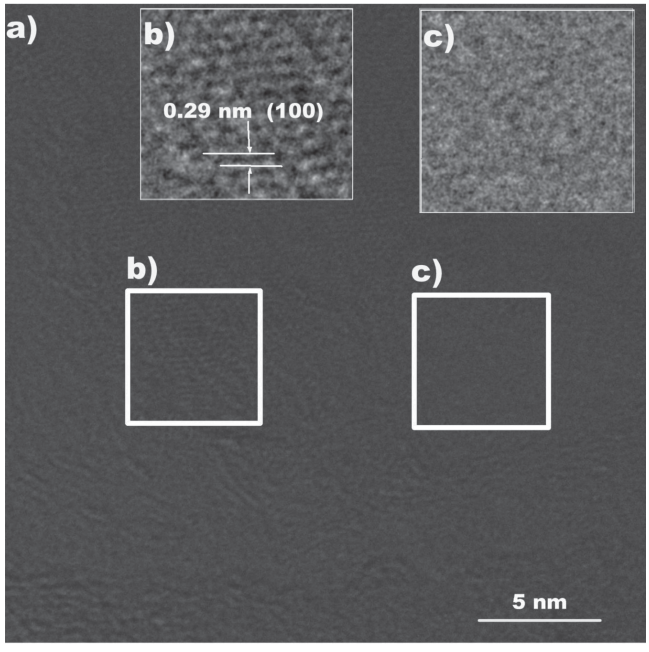

Figure 1. a) High magnification the HRTEM image of the LCMoS_2/RGO hybrid material, b) reconstruction of the HRTEM image showing a region with the MoS_2 single layer, and c) HRTEM image detail showing a region without the MoS_2 layer.

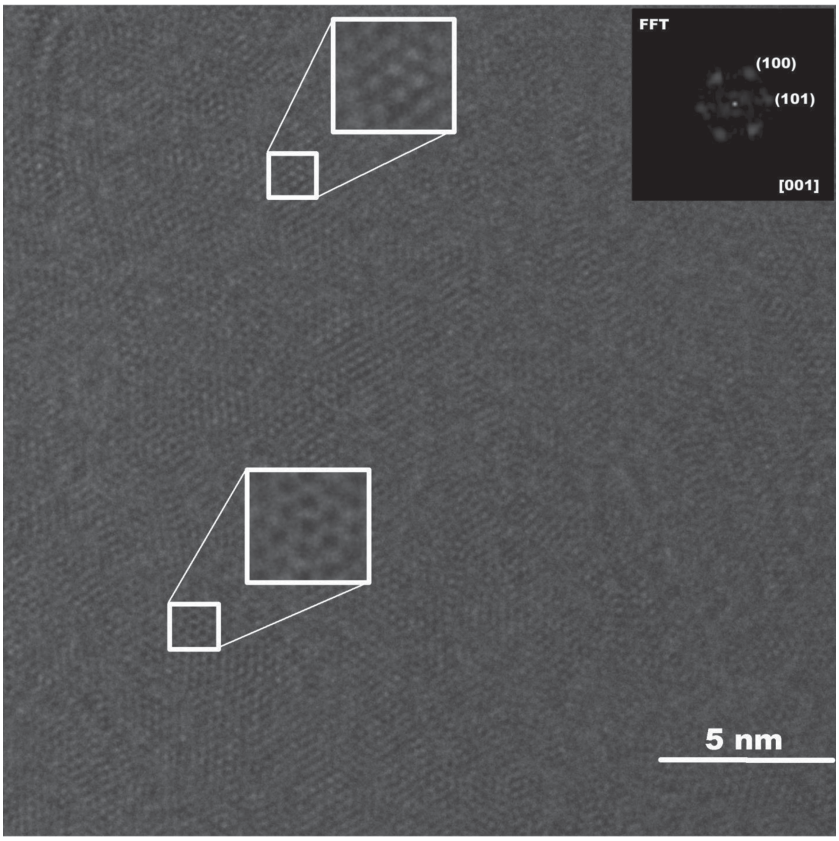

Figure 2. High magnification HRTEM image of the $MCMoS_2$/RGO hybrid material. The inset shows a reconstruction HRTEM image showing regions under-focus and over-focus. The inset shows also a FFT analysis of the under-focus region.

$LCMoS_2$/RGO shows an area covered by single layers of MoS_2 (see Figure 1b) and areas without the sulfide layer (see Figure 1c), which confirms the formation of MoS_2 islands as suggested by the SAED characterization. HRTEM analysis of the $MCMoS_2$/RGO material shows uncorrugated areas and areas with different numbers of dark fringes (see Figure S3 in the Supporting Information). **Figure 2** confirms that a stack of MoS_2 layers forms the uncorrugated area. The insets in Figure 2 exhibit clear symmetry of the MoS_2 hexagonal crystal oriented along [001] zone axes (see inset with the fast Fourier transform (FFT) analysis of the under-focus region). The insets also show a HRTEM image in under-focus and over-focus conditions, which supports the formation of stack layers and steps. **Figure 3** shows a high magnification HRTEM image of the $HCMoS_2$/RGO hybrid material. The predominance of areas with dark fringes (indicated by white arrows) and small corrugated areas are evident; the inset shows a dark fringe in detail. White arrows indicate areas with different numbers of dark fringes. These dark fringes can be associated with the MoS_2 layer folded edges.[28] A semiquantitative analysis of the number of layers can be made by counting the number of fringes. The HRTEM analysis suggests that this hybrid material is formed by 1 to 6 layers of MoS_2. The MoS_2 island in the $LCMoS_2$/RGO material and the stacks of layers and steps in the $MCMoS_2$/RGO were confirmed by atomic force microscopy (AFM) measurements (see **Figure 4**). Figure 4a,d show the AFM analysis of the GO platelet with micrometer-sized homogeneity displayed over the entire lateral dimension. Figure 4c,f show the AFM analysis of the MoS_2/RGO composite ($LCMoS_2$/RGO) where the MoS_2 islands over the RGO are clearly evident, which supports the HRTEM characterization. However, an analysis of the $MCMoS_2$/RGO composite reveals that the MoS_2 entirely covered the RGO platelet (Figure 4b,e). The AFM analysis clearly shows steps on the $MCMoS_2$/RGO and the island in the structure of the $LCMoS_2$/RGO.

To obtain a better chemical description of the hybrid MoS_2/RGO material, we performed XPS analysis of the samples with different [MoS_2]/[RGO] ratios. **Figure 5** shows the Mo 3d region of XPS spectra for $LCMoS_2$/RGO, $MCMoS_2$/RGO and $HCMoS_2$/RGO samples. **Table 1** summarizes the Mo 3d peak position for samples with different [MoS_2]/[RGO] ratios. Mo 3d spectra clearly show two Mo oxidation states where the peaks around 230 eV are related to the Mo $3d_{5/2}$ of Mo^{+4} (typical of the Mo-S bond), and the peaks around 236 eV are related to the Mo $3d_{5/2}$ of Mo^{+6} (typical of the Mo–O bond).[29] Moreover, the peak centered around 233 eV (the mean peak in Figure 5) is the convolution of two peaks related to Mo $3d_{3/2}$ of the Mo–S and Mo–O bonds, which explains the high intensity of this peak. Increasing the [MoS_2]/[RGO] ratio produces a decrease in the peak intensity related to the Mo $3d_{5/2}$ of the Mo–O bond, which suggests that this bond occurs preferentially in the RGO/MoS_2 interface. To verify this hypothesis, we also analyzed the O 1s and S 2p region of the XPS spectra (see Figure S4 in the Supporting Information), which exhibits two peaks: one peak around 531.7 eV related to the Mo-O bond and other peak around 533.6 eV (typical of the C–O bond). The peak around 531.7 eV cannot be associated with MoO_3 phase because the O 1s peak of the MoO_3 phase is expected at 530.6 eV.[30] This chemical shift in the Mo–O bond must be related to a different local chemical environment. The analysis of the S 2p region of XPS spectra (see Figure S5 in the Supporting Information) shows typical peaks of the Mo–S bond (S $2p_{3/2}$ and S $2p_{1/2}$) of the MoS_2 phase. The Fourier transform infrared (FTIR) spectra of the RGO/MoS_2 (see Figure S6 in the Supporting Information) contain bands at the 950 and 850 cm^{-1} characteristics for Mo=O stretching vibrations at the oxosulfide species. The characteristics features in the FTIR spectrum of RGO are the absorption bands corresponding to the C=O carbonyl stretching vibrations at 1700 cm^{-1}, the C–O stretching (epoxy) at 1200 cm^{-1}, and C=C at 1620 cm^{-1} corresponding to the remaining sp^2 character.[31–34] These results support the idea that the Mo–O bond occurs in the RGO/MoS_2 interface and confirms the formation of a covalent bond between the RGO and first MoS_2 layer via the C–O–Mo bond.

Based on the XRD, TEM/HRTEM, AFM, and XPS analyses, we propose the nanostructures illustrated in **Scheme 1**. For a

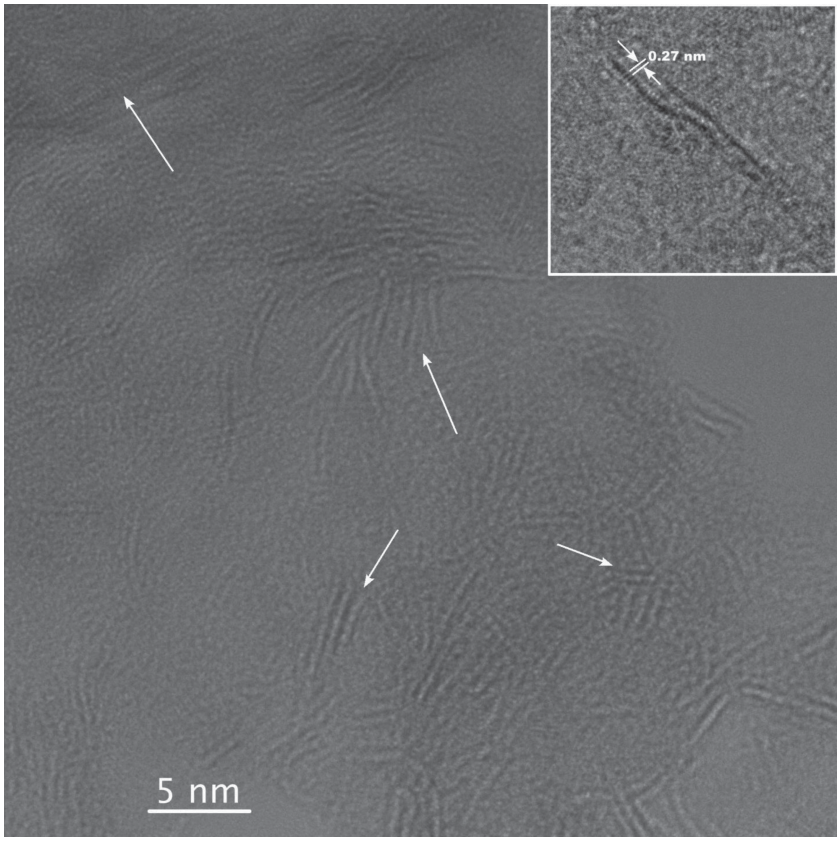

Figure 3. High magnification HRTEM image of the $HCMoS_2$/RGO hybrid material. The inset shows the details of the dark fringe.

low $[MoS_2]$/[RGO] ratio ($LCMoS_2$/RGO), the material is formed by islands of one or more MoS_2 layers deposited on RGO. Increasing the $[MoS_2]$/[RGO] ratio ($MCMoS_2$/RGO) produces complete coverage of the RGO by MoS_2 layers as well as the formation of areas formed by the folded edges of the MoS_2 layer. The uncorregated areas are formed by MoS_2 layers textured along the [001] direction, which results in a structure formed by stacks of layers and steps. The material with the highest concentration of MoS_2 ($HCMoS_2$/RGO) showed a nanostructure predominantly formed by areas of the folded edges of the MoS_2 layer. The bond between the graphene sheet and the MoS_2 layers is predominantly covalent (type C–O–Mo), as illustrated in Scheme 1.

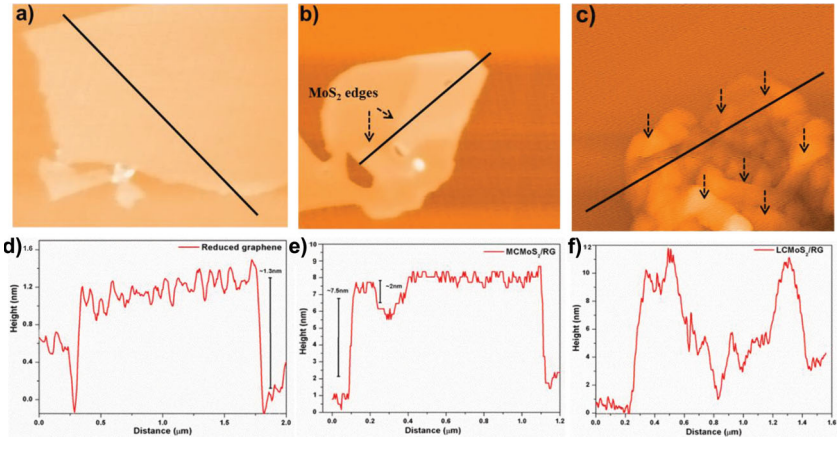

Figure 4. a) AFM image of graphene on mica with flat surface. b) AFM image of $MCMoS_2$/RGO hybrid. c) AFM image of hybrid $LCMoS_2$/RGO with a low concentration of MoS_2 layers. d) Height profile of the image in (a). e) Height profile of the image in (b). f) Height profile of the image in (c).

2.2. MoS_2/RGO as a Supercapacitor (Electrochemical Characterization)

To evaluate the electrochemical performance of MoS_2/RGO hybrids as active supercapacitor electrodes, we performed cyclic voltammetry (CV) and galvanostatic charge/discharge measurements in a three-electrode configuration. A platinum foil and a hydrogen electrode were used as the counter electrode and the reference electrode, respectively, with an aqueous electrolyte (1 M $HClO_4$). As a working electrode, the MoS_2/RGO hybrid material and RGO were deposited on a glassy carbon electrode. CV data for the MoS_2/RGO hybrid material with different $[MoS_2]$/[RGO] ratios at different scan rates (10–80 mV s^{-1}) are shown in **Figure 6**. The plotted CV curves for RGO (at scan rates of 10–80 mV s^{-1}) revealed that the CV curve is a horizontal straight line without any redox peaks, which indicates that RGO possesses only an electrical double-layer capacitance (see Figure S7 in the Supporting Information). The selected potential window for this measurement was chosen for each hybrid material, at a potential higher than the open circuit potential (ocp) to avoid a non-reversible process such as a hydrogen evolution reaction.[1,19] A scanning electron microscopy (SEM) analysis of the working electrode shows the formation of a continuous and rippled film of hybrid material that is formed by a small disc of folded MoS_2/RGO hybrid material (see Figure S8 in the Supporting Information).

As a general trend, the CV curves of MoS_2/RGO hybrid materials (Figure 6) show an increase in the current with a scan rate increase. The CV retains its shape even at high scan rates, indicating a good high-rate performance. The detailed electrochemical results confirm that the CV curves of MoS_2/RGO with a low $[MoS_2]$/[RGO] ratio have a near-rectangular shape indicating quasi-ideal capacitive behavior of the $LCMoS_2$/RGO material (see Figure 6a). A closer look at the $LCMoS_2$/RGO hybrid CV curves reveals very small shoulders that indicate that there are redox processes in this sample. However, the contribution of this faradaic process for the total capacitance is very small. The CV curves

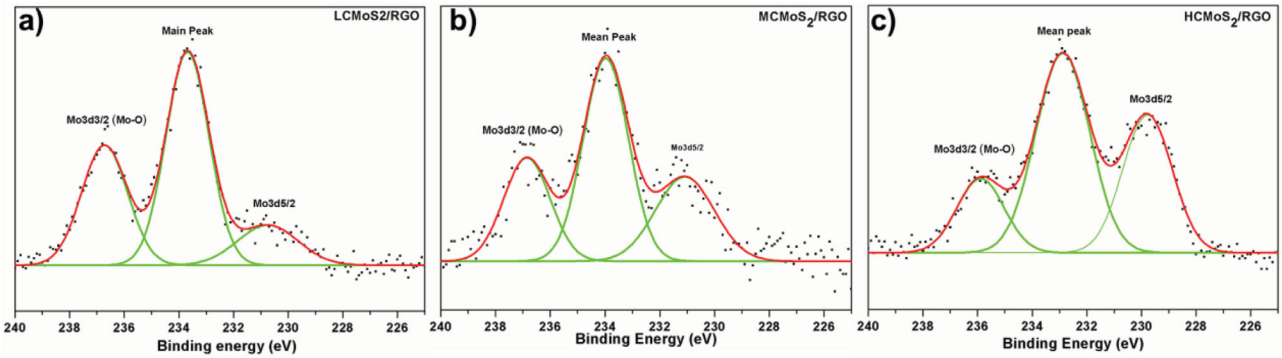

Figure 5. Mo 3d region of the XPS spectra for the hybrid samples: a) $LCMoS_2$/RGO, b) $MCMoS_2$/RGO, and c) $HCMoS_2$/RGO.

Table 1. XPS results Mo 3d peak position for the samples with different [MoS_2]/[RGO] ratios.

	Main peak position [eV]	Mo $3d_{3/2}$ [eV] (Mo-O)	Mo $3d_{5/2}$ [eV] (Mo-S)
$LCMoS_2$/RGO	233.7	236.7	230.7
$MCMoS_2$/RGO	233.9	236.8	231.08
$HCMoS_2$/RGO	232.8	235.9	229.7

(capacitance characteristics) of $MCMoS_2$/RGO and $HCMoS_2$/RGO are distinct. These materials show a combination of a near-rectangular shape voltammogram with reversible peaks that indicate a pseudocapacitive process. The two peaks must be attributed to the oxidation/reduction process of Mo active atoms at the edge of MoS_2 layers (Mo(IV) ⇔ Mo(V) ⇔ Mo(VI)) and are an important contribution to the total capacitance of the hybrid materials.[35] The CV data represent a reversible redox process and suggest excellent electrochemical stability of the hybrid materials.

Specific capacitances of the samples were calculated using the voltammetric charge integration (cathodic current) from the cyclic voltammogram curves and considering the equation $C_s = Q/\Delta Em$ where C_s is the specific capacitance (in farads per gram), Q is the charge of cathodic current (in coulombs), ΔE is the potential window (in volts), and m is the mass of the material in grams. The specific capacitance values calculated for the different materials studied are listed in the Table 1. Although the maximum values obtained are not the best values reported to date, they are 10 times higher than the specific capacitance obtained for a pure MoS_2 thin film measured at 50 mV s^{-1}.[21] In addition, these specific capacitances are also similar to some

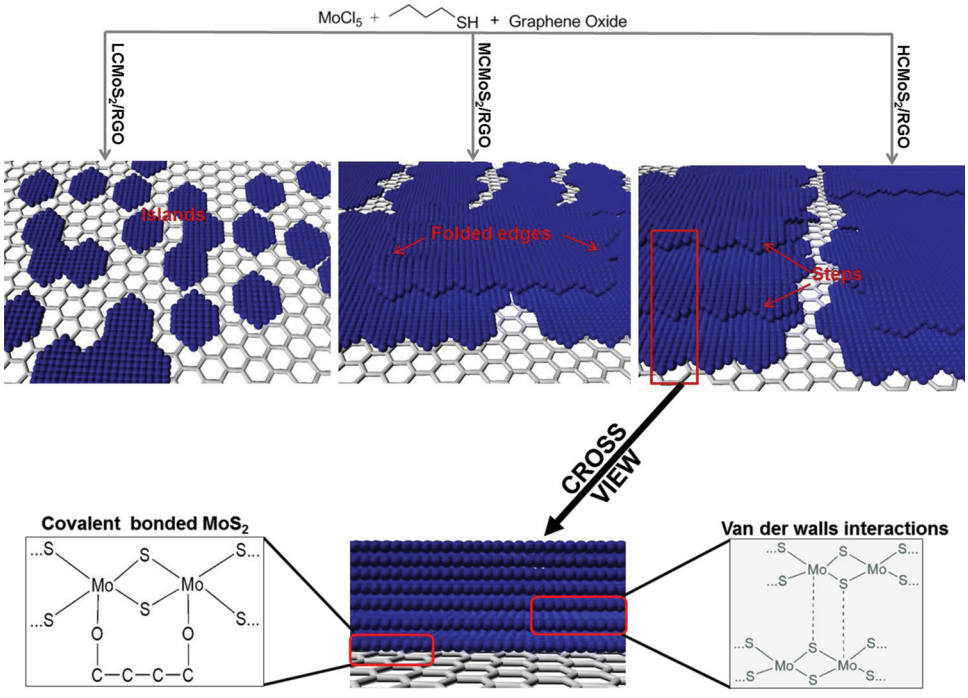

Scheme 1. Preparation of MoS_2/RGO with three concentrations of MoS_2 on reduced graphene oxide, highlighting a schematic cross sectional view of the interaction between MoS_2/MoS_2 layers and between MoS_2 layers/RGO.

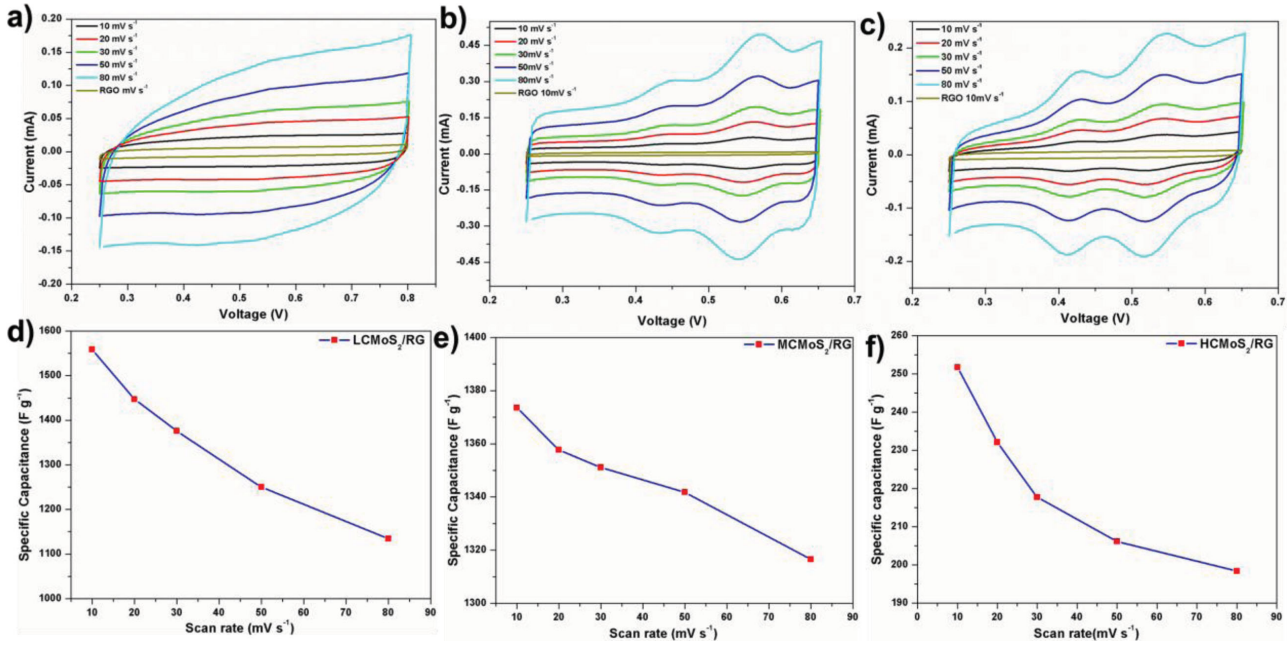

Figure 6. a) Cyclic voltammograms for $LCMoS_2$/RGO hybrid with 5.6 wt% of MoS_2 at different scan rates. b) Cyclic voltammograms for $MCMoS_2$/RGO. c) Cyclic voltammograms for $HCMoS_2$/RGO. d) Specific capacitance (Fg^{-1}) versus scan rates for $LCMoS_2$/RGO. e) Specific capacitance (F g^{-1}) versus scan rates for $MCMoS_2$/RGO. f) Specific capacitance (F g^{-1}) versus scan rates for $HCMoS_2$/RGO. All data were acquired in perchloric acid solution (1 M).

classes of materials investigated as supercapacitor in the literature such as composites (MnO_2/PEDOT ≈ 210 F g^{-1}, RuO_2/graphene ≈ 250 F g^{-1}) or metal oxides (MnO_2 ≈ 260 F g^{-1}, V_2O_5 ≈ 262 F g^{-1}).[36–39]

Galvanostatic charge/discharge curves of $LCMoS_2$/RGO, $MCMoS_2$/RGO and $HCMoS_2$/RGO compared with RGO at three different current densities of 1, 5, and 10 A g^{-1} are shown in **Figure 7**a,b,c. These currents were normalized by the mass of MoS_2 in each hybrid. Charge curves are almost linear and symmetrical to their discharge counterpart, which further indicates the excellent reversibility of MoS_2/RGO composites. The discharging time significantly increases as the MoS_2 loading decreases suggesting that greater MoS_2 loading in the RGO structure produces short charge capacity.

Additionally, the maximum energy storage (E) was calculated according to the equation $E = C_s V^2/2$ where C_s is the specific capacitance (F g^{-1}) and V is the cell voltage (V). The energy densities for the hybrids were calculated to be 63, 29, and 6 W h kg^{-1} for $LCMoS_2$/RGO, $MCMoS_2$/RGO, and $HCMoS_2$/RGO, respectively. The cycling stability of the supercapacitors was performed by CV and provided an excellent electrochemical stability with specific capacitance retention of 92% and 70% for $LCMoS_2$/RGO and $MCMoS_2$/RGO, respectively, after 1000 cycles.

Disregarding any synergetic effect between both materials and considering only MoS_2 as an active material, we estimate the contribution of MoS_2 to the electrochemical performance of the MoS_2/RG electrodes. The specific capacitance of MoS_2 was calculated by subtracting the voltammetric cathodic charge from the value obtained for reduced graphene in the same window potential through the equation $C_{sMoS2} = (Q_{MoS2/RGO} - Q_{RGO})/(\Delta V m_{MoS2})$. Here, $Q_{MoS2/RGO}$ and Q_{RGO} are the voltammetric charge of the MoS_2/RGO and reduced graphene electrodes, respectively. As shown in Figure 6d,e,f, the specific capacitances of MoS_2 increase as the scan rate is decreased from 80 to 10 mV s^{-1} and reach maximum values of 1558, 1373, and 258 F g^{-1}

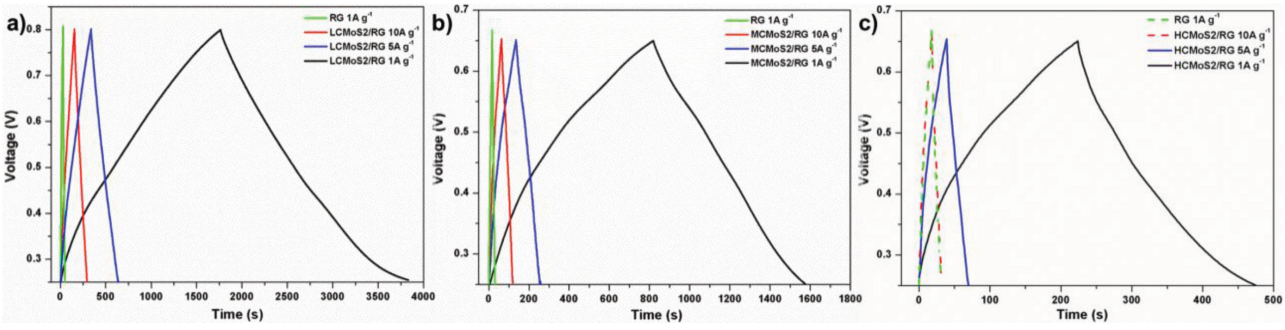

Figure 7. Charge and discharge (voltage versus time) curves at various current density a) $LCMoS_2$/RGO, b) $MCMoS_2$/RGO, and c) $HCMoS_2$/RGO.

Table 2. Specific capacitance values calculated for RGO and hybrids materials.

	Specific capacitance (F g^{-1}) evaluated by total mass of the hybrid		Specific capacitance (F g^{-1}) evaluated by MoS_2 mass values[a)]	
	10 mV s^{-1}	80 mV s^{-1}	10 mV s^{-1}	80 mV s^{-1}
RGO	40	28	–	–
$LCMoS_2$/RGO	128	90	1558	1133
$MCMoS_2$/RGO	265	205	1373	1316
$HCMoS_2$/RGO	148	120	258	198

[a)]These values were evaluated by subtracting the voltametric cathodic charge values to the hybrid from that value obtained for reduced graphene oxide.

for $LCMoS_2$/RGO, $MCMoS_2$/RGO, and $HCMoS_2$/RGO, respectively, at a scan rate of 10 mV s^{-1} (see **Table 2**). These results strongly suggest that the MoS_2 is the active layer of the composite material and redox reactions (pseudocapacitors) or the ion adsorption (electrochemical double layer capacitors) reported in this work must occur in the MoS_2 phase.

Based on structural, morphological, chemical, and electrochemical characterization, we propose a relationship between the storage charge and nanostructure of the hybrid material. The hybrid material revealed that a charge storage controlled by double-layer capacitance ($LCMoS_2$/RGO) is formed by a few layers of MoS_2 covalently bonded to the RGO, which indicates an electrochemical process controlled by the interaction between the electrolyte and the MoS_2 surface. On the other hand, hybrid materials ($MCMoS_2$/RGO and $HCMoS_2$/RGO) with a significant faradaic contribution to the total capacitance are formed by stacks of several layers of MoS_2 (see Scheme 1).

Experimental and theoretical studies related to the adsorption of alkali metals on MoS_2 are associated with the intercalation reaction of alkali metals between the S–Mo–S layers.[40–42] For instance, the intercalation reaction of Li proceeds by reduction of the MoS_2 layers and an insertion of Li^+ cations into the layers of MoS_2 (bonded by van der Walls interactions) for charge compensation. This is accompanied by significant changes in the electronic and crystallographic structure of the host lattice. During the Li intercalation reaction, the semiconductor 2H-MoS_2 undergoes a phase transition to a metastable metallic 1T-MoS_2 polymorph. By analogy, we believe that a similar intercalation reaction occurs in the present work. This hypothesis is supported by the Raman spectra of the $MCMoS_2$/RGO material before and after a charge (intercalation) process (see Figure S9 in the Supporting Information). The material after the intercalation exhibited (Figure S9b, Supporting Information) additional peaks in the lower frequency region. These peaks are ascribed to J_1, J_2, and J_3 modes, which are active in 1T-type MoS_2 but not allowed in 2H-MoS_2.[43] Our results indicate that both phases (1T and 2H) are present in the sample after charge process, supporting the phase transition induced by intercalation.

It is important to emphasize that this electrochemical characterization of hybrids corresponds to a narrow potential window of 0.55 V for $LCMoS_2$/RGO and only 0.4 V for $MCMoS_2$/RGO and $HCMoS_2$/RGO in an aqueous electrolyte. We can speculate that higher specific capacitance values can be achieved by coupling the hybrids to a suitable counter electrode material where a large operating voltage can be reached[44] or by using an organic electrolyte.

3. Conclusion

In summary, we have demonstrated that a previously described simple chemical route yields a MoS_2/RGO hybrid with MoS_2 layers covalently bonded on the surface of the RGO. The characterized morphology of the hybrid (obtained by varying MoS_2 concentrations) provides a suitable material for electrochemical supercapacitor applications where it is possible to highlight electrochemical supercapacitive properties by changing only the MoS_2 concentration for the same hybrid.

4. Experimental Section

Materials: $MoCl_5$ (>95%) and butyl mercaptan $C_4H_{10}S$ (>98%) were purchased from Aldrich Chemical Co. Dimethylformamide (DMF) and ethanol were purchased from Tedia Company, Inc. The graphene oxide (GO) was processed by a modified Hummers method.[45]

Synthesis of the MoS_2/RG Hybrid: All procedures were carried out in a glove box under a controlled atmosphere. In a typical synthesis, 273 mg of $MoCl_5$ and 215 µL of butyl mercaptan were added to a Teflon tube with a colloidal dispersion of GO in DMF (200 mg of GO in 30 mL of DMF). After complete dissolution of the reagents, the sealed tube was removed from the glove box and heated in a MW reactor (Synthos 3000, Anton Paar) at 800 W for 60 min. After the reaction, the product was collected by centrifugation (10 000 rpm for 10 min) and washed with ethanol. This procedure was repeated five times, and then the material was dried in vacuum for several hours. This sample is referred to as a medium concentration of MoS_2 on RGO ($MCMoS_2$/RGO). Two additional reaction tubes were prepared by varying the concentration of precursors. Using the exact same procedure, a low concentration system of MoS_2 on graphene ($LCMoS_2$/RGO) was prepared using 6.9 mg of $MoCl_5$ and 5.5 µL of butyl mercaptan with 200 mg of GO. A high concentration system of MoS_2 on graphene ($HCMoS_2$/RGO) was prepared using 6.9 mg of $MoCl_5$ and 5.5 µL of butyl mercaptan with 200 mg of GO.

Hybrid Characterization: For the HRTEM/energy-dispersive X-ray (EDX) analysis, a TECNAI F20 FEI microscope was used. It was operated at 200 kV. The hybrid composite was dispersed in ethanol and dripped onto a hollow carbon-coated copper grid. For the AFM characterization, the ethanol dispersion of the MoS_2/RGO and RGO was dripped onto a flash cleaved mica substrate. The measurement was performed using Nanosurf Easyscan2 equipment. For SEM images, a FEI Inspect F50 was used. The weight percent of MoS_2 was determined by thermogravimetric analyses in Netzsch STA 409 equipment. XPS measurements were taken in a VG Microtech ESCA3000 spectrometer with a base vacuum of 3×10^{-10} mbar, 250 mm semi-hemispherical analyzer, Al Kα non-monochromatic radiation. Binding energy corrections were made to raw spectra using the C 1s peak at 284. 5 eV.

Electrochemical Characterization: All electrochemical experiments were carried out using a three-electrode configuration on a Metrohm Autolab type III potentiostat. A platinum sheet and hydrogen electrode were used as the counter and reference electrodes, respectively. The electrolyte used is a 1 M $HClO_4$ aqueous solution. The working electrode was prepared by casting a sample onto a glassy carbon electrode with a diameter of 3 mm. Typically, 8 mg of a hybrid was dispersed in 1 mL of an ethanol solution by sonication for 30 min or more. Due to the solubility, the dispersion of the $LCMoS_2$/RGO hybrid was prepared by combining 200 µL of toluene and 800 µL of ethanol; 2 µL of this sample was then dropped onto the glassy carbon electrode (≈0.016 mg) and dried in an oven before the electrochemical test. CV and galvanostatic

charge/discharge tests were used to characterize the electrochemical behavior of supercapacitor electrodes. CV curves were measured in a potential range between 0.25–0.8 V for $LCMoS_2$/RGO and 0.25–0.65 V for $MCMoS_2$/RGO and $HCMoS_2$/RGO at different scan rates. Charge/discharge processes were performed in the same window potential at different current densities. Cyclic stabilities were characterized using CV measurements for over 1000 cycles at a scan rate of 20 mV s^{-1}.

Supporting Information

Supporting Information is available from the Wiley Online Library or from the author.

Acknowledgements

The financial support of FAPESP (2013/02468–0), FINEP, CNPq (INCT program), and CAPES is gratefully acknowledged. This article was modified after online publication to correct errors in the concentrations of $MoCl_5$ and butyl mercaptan that are reported in the Experimental Section for the synthesis of the $HCMoS_2$/RGO hybrid.

Received: September 10, 2013
Revised: October 15, 2013
Published online: November 18, 2013

[1] E. G. S. Firmiano, M. A. L. Cordeiro, A. C. Rabelo, C. J. Dalmaschio, A. N. Pinheiro, E. C. Pereira, E. R. Leite, *Chem. Commun.* **2012**, *48*, 7687.
[2] M. Y. Sun, J. Adjaye, A. E. Nelson, *Appl. Catal. A-Gen.* **2004**, *263*, 131.
[3] M. Chhowalla, G. A. J. Amaratunga, *Nature* **2000**, *407*, 164.
[4] J. Chen, N. Kuriyama, H. Yuan, H. T. Takeshita, T. Sakai, *J. Am. Chem. Soc.* **2001**, *123*, 11813.
[5] A. V. Murugan, M. Quintin, M. H. Delville, G. Campet, C. S. Gopinath, K. Vijayamohanan, *J. Power Sources* **2006**, *156*, 615.
[6] B. Chakraborty, A. Bera, D. V. S. Muthu, S. Bhowmick, U. V. Waghmare, A. K. Sood, *Phys. Rev. B* **2012**, *85*, 161403.
[7] Q. H. Wang, K. Kalantar-Zadeh, A. Kis, J. N. Coleman, M. S. Strano, *Nat. Nanotechnol.* **2012**, *7*, 699.
[8] A. K. Geim, I. V. Grigorieva, *Nature* **2013**, *499*, 419.
[9] H. S. S. R. Matte, A. Gomathi, A. K. Manna, D. J. Late, R. Datta, S. K. Pati, C. N. R. Rao, *Angew. Chem. Int. Ed.* **2010**, *49*, 4059.
[10] K. G. Zhou, N. N. Mao, H. X. Wang, Y. Peng, H. L. Zhang, *Angew. Chem. Int. Ed.* **2011**, *50*, 10839.
[11] M. Bar Sadan, L. Houben, A. N. Enyashin, G. Seifert, R. Tenne, *Proc. Natl. Acad. Sci. USA* **2008**, *105*, 15643.
[12] Y. H. Lee, X. Q. Zhang, W. J. Zhang, M. T. Chang, C. T. Lin, K. D. Chang, Y. C. Yu, J. T. W. Wang, C. S. Chang, L. J. Li, T. W. Lin, *Adv. Mater.* **2012**, 24, 2320.
[13] S. Balendhran, J. Z. Ou, M. Bhaskaran, S. Sriram, S. Ippolito, Z. Vasic, E. Kats, S. Bhargava, S. Zhuiykov, K. Kalantar-Zadeh, *Nanoscale* **2012**, *4*, 461.
[14] C. Altavilla, M. Sarno, P. Ciambelli, *Chem. Mater.* **2011**, *23*, 3879.
[15] Y. Y. Peng, Z. Y. Meng, C. Zhong, J. Lu, W. C. Yu, Y. B. Jia, Y. T. Qian, *Chem. Lett.* **2001**, *8*, 772.
[16] K. Chang, W. X. Chen, *Chem. Commun.* **2011**, *47*, 4252.
[17] K. Chang, W. X. Chen, *ACS Nano* **2011**, *5*, 4720.
[18] H. Hwang, H. Kim, J. Cho, *Nano Lett.* **2011**, *11*, 4826.
[19] Y. G. Li, H. L. Wang, L. M. Xie, Y. Y. Liang, G. S. Hong, H. J. Dai, *J. Am. Chem. Soc.* **2011**, *133*, 7296.
[20] Y. D. Ma, Y. Dai, M. Guo, C. W. Niu, B. B. Huang, *Nanoscale* **2011**, *3*, 3883.
[21] J. M. Soon, K. P. Loh, *Electrochem. Solid State* **2007**, *10*, A250.
[22] L. Cao, S. Yang, W. Gao, Z. Liu, Y. Gong, L. Ma, G. Shi, S. Lei, Y. Zhang, S. Zhang, R. Vajtai, P. M. Ajayan, *Small* **2013**, *9*, 2905.
[23] W. Y. Li, Q. Liu, Y. G. Sun, J. Q. Sun, R. J. Zou, G. Li, X. H. Hu, G. S. Song, G. X. Ma, J. M. Yang, Z. G. Chen, J. Q. Hu, *J. Mater. Chem.* **2012**, *22*, 14864.
[24] X. Y. Lang, A. Hirata, T. Fujita, M. W. Chen, *Nat. Nanotechnol.* **2011**, *6*, 232.
[25] Y. W. Zhu, S. Murali, W. W. Cai, X. S. Li, J. W. Suk, J. R. Potts, R. S. Ruoff, *Adv. Mater.* **2010**, *22*, 5226.
[26] S. Baek, S. H. Yu, S. K. Park, A. Pucci, C. Marichy, D. C. Lee, Y. E. Sung, Y. Z. Piao, N. Pinna, *RSC Adv.* **2012**, *2*, 13038.
[27] W. F. Chen, L. F. Yan, P. R. Bangal, *Carbon* **2010**, *48*, 1146.
[28] J. Brivio, D. T. L. Alexander, A. Kis, *Nano Lett.* **2011**, *11*, 5148.
[29] A. Khademi, R. Azimirad, A. A. Zavarian, A. Z. Moshfegh, *J. Phys. Chem. C* **2009**, *113*, 19298.
[30] J. G. Choi, L. T. Thompson, *Appl. Surf. Sci.* **1996**, *93*, 143.
[31] T. Weber, J. C. Muijsers, H. J. M. C. van Wolput, C. P. J. Verhagen, J. W. Niemantsverdriet, *J. Phys. Chem.* **1996**, *100*, 14144.
[32] A. B. Bourlinos, D. Gournis, D. Petridis, T. Szabo, A. Szeri, I. Dekany, *Langmuir* **2003**, *19*, 6050.
[33] S. Stankovich, R. D. Piner, S. T. Nguyen, R. S. Ruoff, *Carbon* **2006**, *44*, 3342.
[34] J. I. Paredes, S. Villar-Rodil, A. Martinez-Alonso, J. M. D. Tascon, *Langmuir* **2008**, *24*, 10560.
[35] S. P. Vincent, *Biochem. J.* **1979**, *177*, 757.
[36] R. Liu, S. B. Lee, *J. Am. Chem. Soc.* **2008**, *130*, 2942.
[37] Z. S. Wu, D. W. Wang, W. Ren, J. Zhao, G. Zhou, F. Li, H. M. Cheng, *Adv. Funct. Mater.* **2010**, *20*, 3595.
[38] X. H. Yang, Y. G. Wang, H. M. Xiong, Y. Y. Xia, *Electrochim. Acta* **2007**, *53*, 752.
[39] Z. J. Lao, K. Konstantinov, Y. Tournaire, S. H. Ng, G. X. Wang, H. K. Liu, *J. Power Sources* **2006**, *162*, 1451.
[40] V. Alexiev, R. Prins, T. Weber, *Phys. Chem. Chem. Phys.* **2000**, *2*, 1815.
[41] G. Eda, H. Yamaguchi, D. Voiry, T. Fujita, M. Chen, M. Chhowalla, *Nano Lett.* **2011**, *11*, 5111.
[42] M. A. Lukowski, A. S. Daniel, F. Meng, A. Forticaux, L. Li, S. Jin, *J. Am. Chem. Soc.* **2013**, *135*, 10274.
[43] S. J. Sandoval, D. Yang, R. F. Frindt, J. C. Irwin, *Phys. Rev. B* **1991**, *44*, 3955.
[44] Z. Fan, J. Yan, T. Wei, L. Zhi, G. Ning, T. Li, F. Wei, *Adv. Funct. Mater.* **2011**, *21*, 2366.
[45] W. S. Hummers, R. E. Offeman, *J. Am. Chem. Soc.* **1958**, *80*, 1339.